In-plane magnetic structure and exchange interactions in the high-temperature antiferromagnet Cr_2Al

Chengxi Zhao [1], Kisung Kang,[1] Joerg C. Neuefeind [2], André Schleife [1,3], and Daniel P. Shoemaker [1,*]

[1]*Department of Materials Science and Engineering and Materials Research Laboratory,*
University of Illinois at Urbana-Champaign, Urbana, Illinois 61801, USA
[2]*Neutron Scattering Division, Oak Ridge National Laboratory, Oak Ridge, Tennessee 37831, USA*
[3]*National Center for Supercomputing Applications, University of Illinois at Urbana-Champaign, Urbana, Illinois 61801, USA*

The ordered tetragonal intermetallic Cr_2Al forms the same structure type as Mn_2Au, and the latter has been heavily investigated for its potential in antiferromagnetic spintronics due to its degenerate in-plane Néel vector. We present the single-crystal flux growth of Cr_2Al and orientation-dependent magnetic properties. Powder neutron diffraction of Cr_2Al and first-principles simulations reveal that the magnetic ordering is likely in-plane and therefore identical to Mn_2Au, providing a second material candidate in the $MoSi_2$ structure type to evaluate the fundamental interactions that govern spintronic effects. The single ordering transition seen in thermal analysis and resistivity indicates that canting of the moments along the c axis is unlikely. Magnetometry, resistivity, and differential scanning calorimetry measurements confirm the Néel temperature to be 634 ± 2 K. First-principles simulations indicate that the system has a small density of states at the Fermi energy and confirm the lowest-energy magnetic ground-state ordering, while Monte Carlo simulations match the experimental Néel temperature.

I. INTRODUCTION

Antiferromagnets have attracted considerable attention due to fundamentally different proposed magnetization switching mechanisms and optically-probed spin-relaxation dynamics in the THz range [1–3], compared with GHz for ferromagnets and ferrimagnets [4–7]. Recent studies have demonstrated partial switching of the Néel vector of antiferromagnetic CuMnAs and Mn_2Au [8–10], perhaps due to current-induced spin-orbit torques [11–15]. The magnetic-field-induced spin rotation and spin-flop behavior of epitaxial CuMnAs thin films has been probed using x-ray magnetic linear dichroism, and signatures of the Néel vector reorientation have been seen in the anisotropic magnetoresistance with multiterminal devices [11,14,16]. Néel vector reorientations have also been observed in femtosecond pump-probe magneto-optical Kerr effect experiments [12].

Intriguingly, Chien *et al.* have shown that the purported spin-orbit torque magnetoresistance effects may be artifacts of excessive current-induced heating through multiterminal devices, thus unequivocal detection of the Néel vector before and after spin-orbit torque switching at low currents is required to effectively prove magnetic switching [17]. The in-plane current-pulse switching experiments on Mn_2Au quantified the anisotropic magnetoresistance and planar Hall effect of thin films [18]. A spin-orbit-torque-driven antiferromagnetic resonance of Mn_2Au has not been observed to date by time-domain THz spectroscopy, despite early reports [19].

Mn_2Au remains antiferromagnetic until it forms a disordered (Mn,Au) solid solution at 953 K [20], with a Néel temperature predicted to be above 1600 K due to its large anisotropy energy, calculated from first-principles calculations [21]. Such large anisotropy may not be desired in all spintronic applications. In particular, the ability to observe a Néel-order-driven effect vanish at T_N without excessive current flow and Joule heating would be a strong confirmation of true spintronic effects. To understand the underlying physics and capabilities, there is a pressing need to expand the library of intermetallic antiferromagnets that share features with CuMnAs (which itself has not been grown as bulk single crystals, likely due to a competing orthorhombic phase) [22] and Mn_2Au. Single crystals of such materials are needed to study the orientation dependence of their magnetic dynamics.

Cr_2Al is an incongruently-melting intermetallic antiferromagnet with the $MoSi_2$ structure type, tetragonal space group $I4/mmm$, isostructural to Mn_2Au and Au_2Mn. There is no reported single crystal growth or measurements of its anisotropic properties. Atoji presented variable-temperature powder neutron diffraction of Cr_2Al in 1965 [23]. In that study, the (001) neutron-diffraction peak intensity was used to determine the $T_N = 598 \pm 5$ K. The magnetic structure was claimed to be inclined by an angle $65 \pm 2.4°$ toward the c axis, although no explanation of that determination was given. The magnetic configuration is shown in Fig. 1. We show here that the in-plane (zero canting) spin configuration is more plausible.

In 1988, Semukhin *et al.* investigated the magnetic phase transition of Cr_2Al by high-temperature x-ray diffraction and calorimetry [24]. Sharp changes in the a and c axis lattice
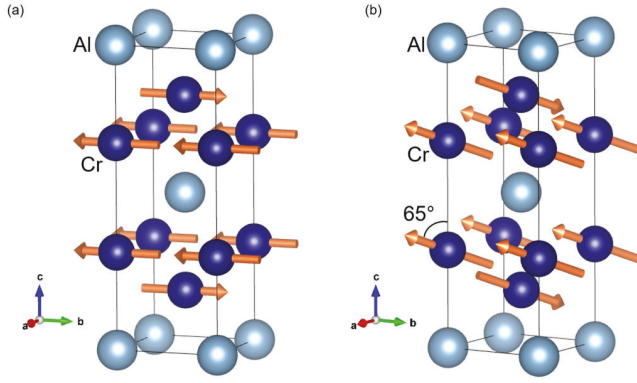
*dpshoema@illinois.edu

FIG. 1. The $k = 0$ magnetic structure of Cr_2Al is shown in panel (a), with Al light and Cr dark. The reported magnetic structure from Atoji in panel (b) has a $65°$ canting away from the c axis [23]. No data in our study point to a reduction in symmetry from our in-plane model to that of Atoji.

parameters and a heat-capacity anomaly occurred at 655 ± 5 K. Variation in the reported T_N may be due to a compositional width of the Cr_2Al phase, which has been reported to be about 10% [25,26]. Variable T_N can also arise from further alloying, as when Susner *et al.* showed that the resistivity anomaly at T_N shifts to lower temperatures and is more pronounced with increased Fe substitution for Cr [27].

Here we show the first steps of understanding the potential of Cr_2Al as a spintronic material, with single crystal growth via tin flux and melt decanting. We consider the allowed magnetic orderings and examine the sensitivity to a c-axis component of the local moments. Magnetometry measurements with varying temperature and external field show the predicted magnetic susceptibility and anisotropy, while resistivity and calorimetry confirm the presence of a single T_N, without a second metamagnetic transition that would be expected in the case of spin canting as proposed by Atoji [23]. First-principles simulations test multiple magnetic configurations, with the experimental ordering found to be the predicted ground state. Exchange coefficients and band structures show how Cr_2Al has a small density of states near the Fermi energy and confirm the experimental susceptibility and T_N.

II. METHODS

Tetragonal single crystals with edge lengths around 0.5 mm and mass 1–2 mg were grown from Sn flux. Cr (>99.99% metals basis) and Al (99.9999% metals basis) powders were mixed in 2 : 1.5 molar ratio along with 95 mol% Sn powder (99.98% metals basis) inside an Ar-filled glove box and vacuum sealed inside a 13 mm inner diameter quartz tube. A stainless-steel mesh was inserted inside the tube just above the powder mixture. The tube was heated to 1173 K at 10 K/min and held for 12 hours, slowly cooled to 933 K at 2 K/hr, and then the tube was taken out, flipped, and centrifuged to filter the grown crystals with the inserted mesh, followed by an air quench to room temperature. The collected crystals were sonicated in 1 M nitric acid for two hours to remove residual Sn. Separately, Cr_2Al powder was prepared by annealing a

mixture of Cr and Al powders with molar ratio of 2 : 1 that was pressed into a pellet and heated at 1073 K for 72 hours.

Scanning electron microscopy was performed in a JEOL 6060 LV SEM, and x-ray diffraction was performed in a Bruker D8 ADVANCE diffractometer with Mo $K\alpha$ radiation. Powder neutron diffraction was performed on the NOMAD instrument at the Spallation Neutron Source at Oak Ridge National Laboratory [28]. Nuclear and magnetic structures were refined using GSAS-II [29] and structures were visualized using VESTA [30]. After alignment by x-ray diffraction (XRD), single-crystal magnetometry was conducted using a standard quartz rod (2 to 400 K) and oven attachment (up to 750 K) on a Quantum Design MPMS3 vibrating sample magnetometer. High-temperature resistivity up to 773 K was measured using the two-point pressed contact configuration shown in Fig. S1 of the Supplemental Material [31]. A separate thermocouple was placed on the sample stage to measure the temperature and the measurement was performed under a flowing nitrogen atmosphere. Differential scanning calorimetry was performed with 2.5 mg of crystals on a TA DSC 2500.

First-principles density-functional theory (DFT) simulations were performed using the Vienna *Ab Initio* Simulation Package [32,33] (VASP). In solving the Kohn-Sham equation, we used the generalized-gradient approximation (GGA) formulated by Perdew, Burke, and Ernzerhof [34], to describe exchange and correlation. The electron-ion interaction was described by the projector-augmented wave [35] (PAW) method. For the Brillouin-zone sampling, $21 \times 21 \times 7$ Monkhorst-Pack (MP) [36] **k** points were used. The kinetic-energy cutoff of the plane-wave basis was chosen as 600 eV by convergence testing. Phonon dispersion calculations within the finite displacement method were performed using the PHONOPY package [37], a supercell of $3 \times 3 \times 1$, and a $4 \times 4 \times 4$ MP **k**-point grid. We performed all-energy dispersion calculations accounting for noncollinear magnetism and spin-orbit coupling [38].

Exchange coefficients are calculated using the spin polarized relativistic Korringa-Kohn-Rostoker (SPR-KKR) code [39] and the relaxed atomic structure from the DFT calculations described above. To integrate over the Brillouin zone, 1000 randomly chosen k points are used in our energy convergence test with a criterion of 0.01 meV/atom. Next, the exchange coefficients are extracted by Lichtenstein's approach, as implemented in the SPR-KKR code [40]. The exchange coefficients follow from the isotropic exchange term in a Heisenberg model,

$$\mathcal{H}_{ex} = -\sum_{i \neq j} J_{ij} e_i e_j. \quad (1)$$

The exchange Hamiltonian $\mathcal{H}_{ex}$ consists of isotropic exchange coefficients J_{ij} and the unit vector of all magnetic moments at sites i and j (e_i and e_j). J_{ij} is calculated up to a relative interaction distance $d = 4.0a$, where a is the a axis lattice parameter of Cr_2Al.

We calculate atomistic spin dynamics using a Monte Carlo approach implemented in UPPASD [41] to estimate the Néel temperature. To simulate microscopic magnetism at finite temperature, the stochastic Landau-Lifshitz-Gilbert (LLG)
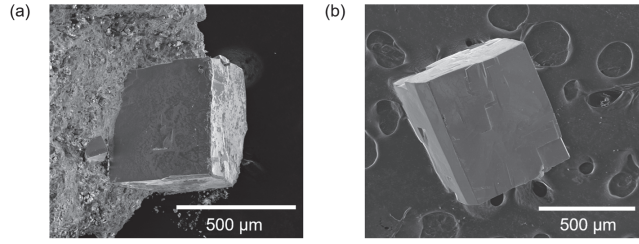
FIG. 2. SEM micrographs of Cr_2Al crystals grown from Sn flux, after centrifuging and (a) before and (b) after removal of Sn with 1 M nitric acid.

FIG. 3. X-ray diffraction data for Cr_2Al crystals are shown for (a) multiple crystals collected simultaneously, along with a Rietveld-refined model for a powder. The asterisked peak is from the paraffin wax mount. In panel (b), data are shown for a single crystal oriented in three orthogonal directions and collected with the sample stationary. Insets show the measurement configurations with crystals loaded in Kapton capillaries.

equation [41] is solved,

$$\frac{d\mathbf{m}_i}{dt} = -\gamma_L \mathbf{m}_i \times \left(\mathbf{B}_i + \mathbf{B}_i^{fl}\right)$$
$$-\gamma_L \frac{\alpha}{m_i} \mathbf{m}_i \times \left[\mathbf{m}_i \times \left(\mathbf{B}_i + \mathbf{B}_i^{fl}\right)\right], \quad (2)$$

where α is an isotropic Gilbert damping constant and $\gamma_L = \gamma/(1+\alpha^2)$ is the renormalized gyromagnetic ratio. $\mathbf{m}_i$ is the magnetic moment at site i and here we use the value from our DFT ground-state simulations. $\mathbf{B}_i$ is the effective magnetic field containing exchange, anisotropy, and magnetic dipolar interactions at magnetic site i. The stochastic term is introduced by the thermally fluctuating magnetic-field term $\mathbf{B}_i^{fl}$. This term is a Gaussian distribution with zero mean and a variance that depends on temperature, based on a central limit theorem. All atomistic spin dynamics calculations use a $12 \times 12 \times 4$ supercell.

III. RESULTS AND DISCUSSION

The crystals obtained from melt centrifuging were metallic silver and had rectangular prismatic shapes, with a typical appearance shown in Fig. 2, before and after etching excess Sn in nitric acid. The phase purity was confirmed by powder XRD of several aligned crystals in a capillary and measured while rotating, which gives peaks that more fully reproduce the powder pattern of Cr_2Al in Fig. 3(a), with some expected difference in peak intensity due to preferred orientation. Collection of XRD data on stationary single crystals was used to determine the direction of the c axis, with XRD shown for a typical crystal measured on three orientations shown in Fig. 3(b). Energy-dispersive x-ray spectroscopy gave an average Cr : Al ratio of 2.0(2), shown in Fig. S2 of the Supplemental Material [31].

Figures 4(a) and 4(b) show the neutron-diffraction pattern of Cr_2Al powder at 298 K. The nuclear peaks give a clear fit to the ordered $I4/mmm$ structure, with the magnetic peak (001) clearly visible at $d = 8.65$ Å. The magnetic propagation vector $k = (000)$ reproduces all magnetic peaks, which confirms that the magnetic unit cell exhibits the same dimension as the crystallographic unit cell. The magnetic space group of Cr_2Al with the Néel vector along [100] is P_Innm in Belov-Neronova-Smirnova (BNS) notation and $I_Pm'm'm$ in Opechowski-Guccione (OG) notation, and the refinement in Fig. 4 is thus constrained with Cr1 moments on the body center sites opposite to the Cr2 moments on the edges of the cell.
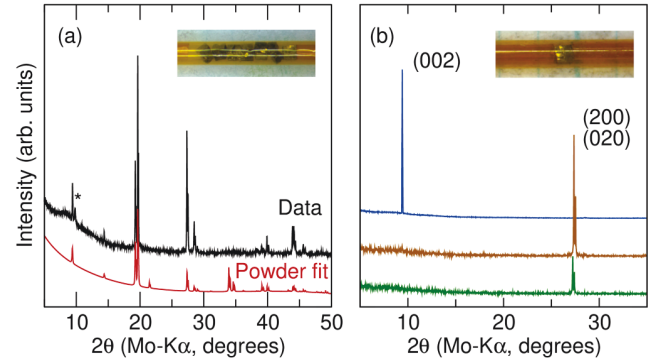
The refined magnetic moments on Cr positions are $1.06(19)\mu_B$. The obtained magnetic structure is visualized in Fig. 1(a). Powder diffraction is not sensitive to the orientation of the Cr moments within the ab plane. The refined structure, with bilayers of Cr normal to c that are ferromagnetic within each layer but antiferromagnetic across the two layers, gives a significantly improved fit over a model where the Cr bilayers have ferromagnetic alignment within and across both layers, or antiferromagnetic alignment from layer to layer. These fits to the neutron-diffraction data are shown in Figs. S4 and S5 of the Supplemental Material [31]. The latter configurations relax to a nonmagnetic state in first-principles simulations. Likewise, a uniaxial configuration with spins along c does not reproduce the neutron data (Figs. S6–S8 of the Supplemental Material [31]). A small canting of the moments toward c, as suggested by Atoji [23], does not significantly improve the fit, even with the addition of an extra free parameter, as shown in Fig. S9 of the Supplemental Material [31]. Small canting is, thus, unlikely due to the additional irreducible representation that would be required to observe it, along with the presence of a single Néel transition, which we discuss subsequently. Canting the moment along c also leads to a calculated increase in the total energy, as shown in Fig. S10 of the Supplemental Material [31].

First-principles density-functional theory simulations for antiferromagnetic Cr_2Al are implemented for ground-state calculations, electronic band structure, phonon dispersion, magnetic susceptibility, and exchange coefficients. The calculated ground state confirms the $I4/mmm$ structure with $a = 2.98$ Å and $c = 8.63$ Å, in good agreement with the room-temperature lattice parameters $a = 3.00$ Å and $c = 8.65$ Å from neutron diffraction in Fig. 4. Magnetic moments on Cr sites shown in Fig. 4 converged to $1.311\mu_B$. The discrepancy of 23% likely arises from decrease of the low-temperature moment upon heating to 300 K. Ground-state DFT simulations for other possible magnetic orderings (see Figs. S4 and S5) [31] conclude that there is no stable state for those configurations.
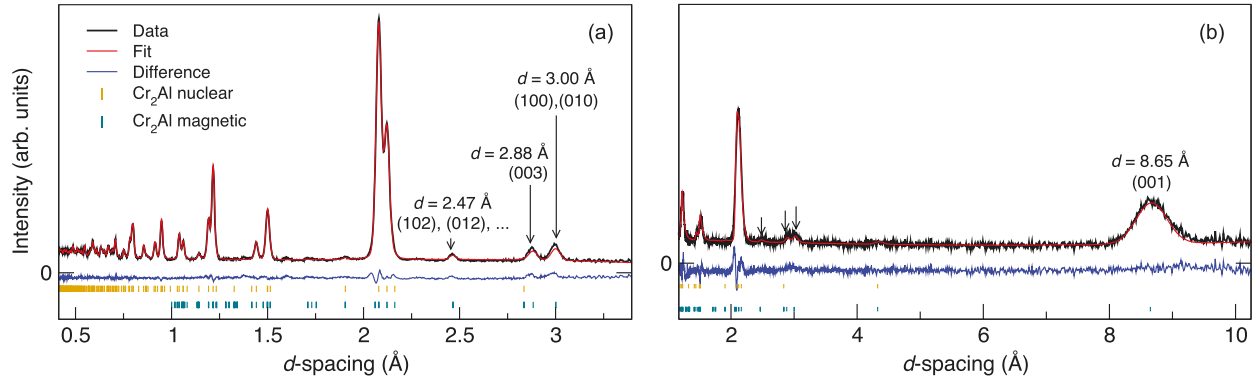
FIG. 4. Time-of-flight neutron-diffraction patterns and Rietveld-refined patterns from NOMAD detector banks with average collection angles (a) $2\theta = 65°$ and (b) $2\theta = 15.1°$. The two banks are optimized for collection on different ranges of d spacings. Orange and blue tick marks indicate nuclear and magnetic peaks, respectively. Magnetic peaks are indicated by arrows and indexing.

The temperature dependence of the magnetic susceptibility of an aligned single crystal from 430 to 750 K with $H = 1$ T is shown in Fig. 5(a). A small hump is observed at $T_N = 634$ K for measurements with $H||a$ and $H||c$. The splitting of the two orientations and the lower susceptibility with field along a indicates that the magnetic ordering is in the ab plane. Further confirmation of T_N is seen in calorimetry, shown in Fig. 5(b). The small event at $T = 505$ K is the melting of a small amount of residual Sn. The fraction of residual Sn is estimated to be 2 wt% based on peak integration of the DSC measurement (see Fig. S11) [31,42].

The magnetization as a function of applied field and orientation is shown in Fig. 6. The anisotropy consistently shows

that the susceptibility along c is greater than along a, which is to be expected for moments lying in the ab plane. No evidence of a spin-flop transition is observed up to $H = 7$ T. When the temperature of the experiment is raised to 750 K, the anisotropy between c and a directions vanishes, as expected above T_N. This is the first measurement of the magnetic anisotropy of a bulk $MoSi_2$-type antiferromagnet in the vicinity of its T_N, and understanding the temperature dependence will be a crucial topic of future work.

The phenomenon that the measured moment of Cr_2Al is greater with $H||c$ over the entire field and temperature range can be compared with similar measurements on another in-plane degenerate antiferromagnet Fe_2As [43]. In Fe_2As, the
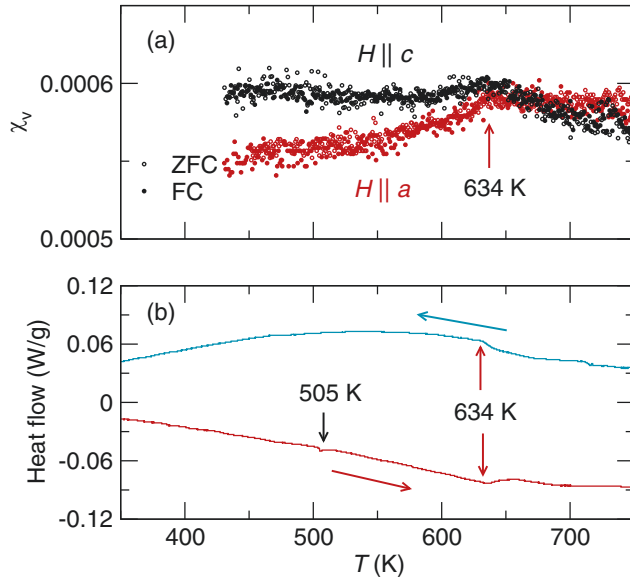

FIG. 5. The temperature dependence of (a) Cr_2Al dimensionless magnetic susceptibility χ under an applied field $H = 1$ T, measured to 750 K. Zero-field-cooled (ZFC) and field-cooled (FC) measurements, represented as open and filled circles, overlap in both crystal orientations. In panel (b), DSC measurements of multiple crystals confirm T_N, with a small anomaly at the Sn melting temperature of 505 K.
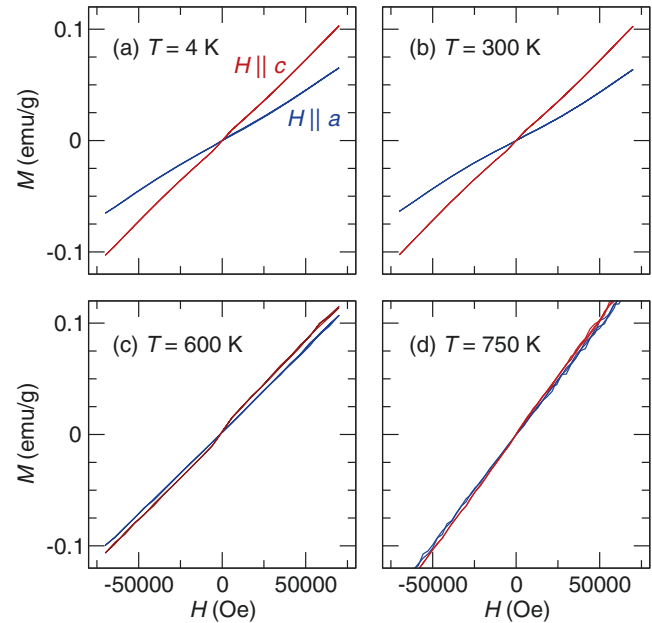

FIG. 6. (a)–(d) Field-dependent magnetization of Cr_2Al at $T = 4$, 300, 600, and 750 K, shown for field along the a (blue) and c axes (red). Anisotropy in the susceptibility vanishes above $T_N \approx 634$ K. (a) $T = 4$ K, (b) $T = 300$ K, (c) $T = 600$ K, and (d) $T = 750$ K, with H along the a axis (blue line) and H along the c axis (red line).
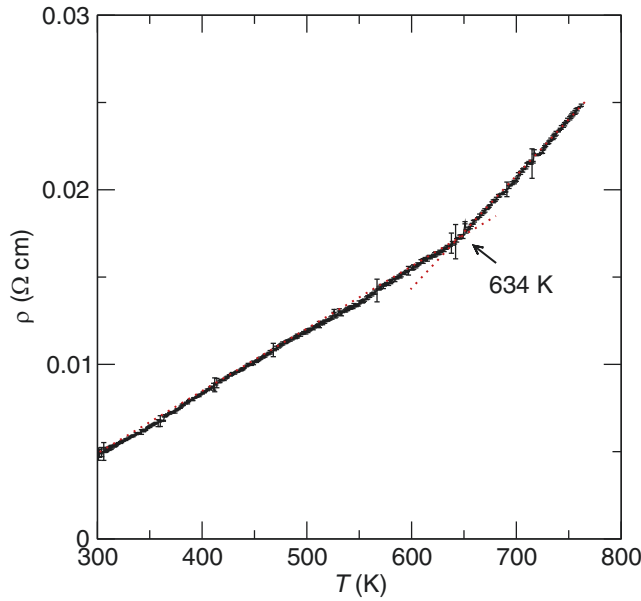
FIG. 7. Two-point resistivity measurement of an unaligned Cr_2Al polycrystal shows a clear transition at T_N, measured under flowing N_2.

FIG. 8. (a) Electronic band structure and total and projected density of states of Cr_2Al and (b) magnified band structure near the Fermi level.

low-field susceptibility mirrors that of Cr_2Al. Above approximately 0.7 T, the susceptibility of Fe_2As with $H||a$ becomes greater than with $H||c$, indicating rotation of the antiferromagnetic domains into a single-domain state with all moments likely along b. This domain rotation is absent in Cr_2Al for the fields we are able to achieve here. This lack of domain rotation is most likely due to the small intrinsic susceptibility of Cr_2Al versus Fe_2As.

The magnetic susceptibility of Cr_2Al can be extracted from total-energy calculations within DFT for magnetic configurations with tilted magnetic moments. Since an explicit magnetic field is not implemented in our DFT simulations, we use the tilting of magnetic moments to mimic the magnetic structure under an applied external field [44]. Within this approach, we obtain the lowest energy for a given tilting angle. Constraining the tilting angle of magnetic moments changes the total energy due to exchange interactions in the tilted state (see Fig. S10 [31]). We compute the magnetic susceptibility from a quadratic fit to the resulting total-energy curve and the equation

$$\chi_v = \frac{\mu_0}{2a - \mu_0}, \tag{3}$$

where μ_0 is the vacuum permeability and a the quadratic fit coefficient [44]. Since DFT implements the calculation at $T = 0$ K, χ_a should be zero and χ_c is nonzero for a single crystal with a single domain. Thus, we assume an experiment in which the field is oriented along the c axis and moments are tilted within the ac plane. The calculated magnetic susceptibility χ_c^{DFT} is 6.88×10^{-4}, which shows good agreement with the scale of measured value of 1.07×10^{-4} at $T = 4$ K, two orders of magnitude smaller than 0.015 for Fe_2As [43].

The two-point resistivity of Cr_2Al from 298 to 733 K is shown in Fig. 7. Since contact resistance between the Al pads and the Cr_2Al sample is present, these data serve as an upper
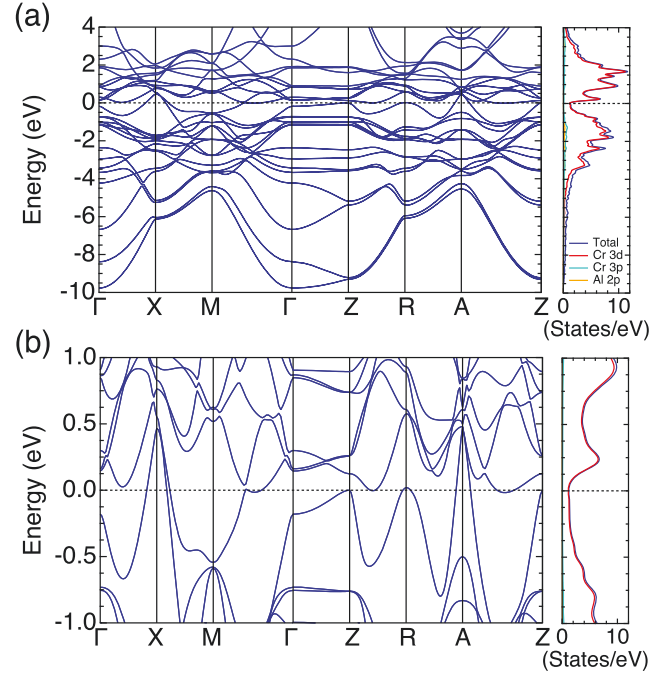
bound for the intrinsic resistivity of Cr_2Al. A clear second-order transition can be observed at 634 K where the slope $d\rho/dT$ increases, indicating an increase in scattering due to the disappearance of AF domains.

The calculated electronic band structure shown in Fig. 8 demonstrates the metallicity of Cr_2Al, with a low electronic density of states near the Fermi level, which leads to high resistivity, especially when some antisite defects may be present due to the compositional phase width of Cr_2Al. The number of states at the Fermi level of Cr_2Al is 0.0155 states/(eV Å), smaller than that of Fe_2As [0.0770 states/(eV Å)] [45]. This explains why Cr_2Al shows higher resistivity than Fe_2As. The projected density of states shows that a wide energy range of states originates from Cr $3d$ orbitals, while s or p orbital contributions from Cr and Al are small.

The structural stability of Cr_2Al is confirmed by the phonon dispersion, computed using the finite difference method including the antiferromagnetic configuration and the effect of spin-orbit coupling, shown in Fig. 9. There are no states with imaginary energy or frequency, which confirms the dynamic stability. There are a total of 18 phonon bands, spanning the energy up to 50 meV. The phonon density of states shows two peaks around 30 and 45 meV.

Exchange coefficients describe the interaction between magnetic moments and can further explain the magnetic structure of Cr_2Al. These exchange coefficients can be utilized for atomistic spin dynamics simulations, as has been done for Fe_2As [46]. The exchange coefficients extracted in this work are shown as a function of relative distance (d/a) in Fig. 10. Positive and negative exchange parameters indicate ferromagnetic and antiferromagnetic couplings, respectively. The nearest-neighbor exchange interaction ($J1 =$
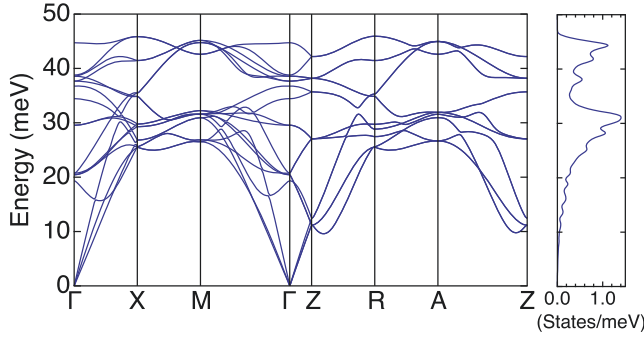
FIG. 9. Phonon bands and density of states of Cr_2Al calculated by the finite-difference method and DFT.

-18.5 meV, shown as a yellow arrow in Fig. 10) is the primary driving force for the AF ordering in Cr_2Al. Even though the third-nearest-neighbor exchange interaction also shows a negative value ($J3 = -3.1$ meV), the corresponding moments show parallel alignment. This is because the $J3$ interaction is overcompensated by $J5 = +2.2$ meV, i.e., ferromagnetic coupling, which has a multiplicity four, while $J3$ has only one interaction. Interactions along a and b directions are all ferromagnetic ($J2 = +0.9$ meV and $J4 = +0.9$ meV). Numerical uncertainties of the exchange integrals mainly originate from k-point sampling and we determined these to be lower than 2.7%, except for $J4$, where due to the small absolute value the relative error is larger (14.2%).

Based on the calculated exchange coefficients, T_N was estimated using three thermodynamic observables that were computed from Monte Carlo (MC) simulations, see details in Ref. [41]. The observables, computed using the stochastic LLG equation, are shown as a function of T in Fig. 11. Sublattice magnetization (M_{sub}, black solid line) is not sharp enough to determine the critical temperature because of finite-size effects, but it does reproduce the 23% difference between the calculated $T = 0$ K M_{sub} and the experimental M_{sub} at 300 K from neutron scattering. Instead, we use the Binder cumulant
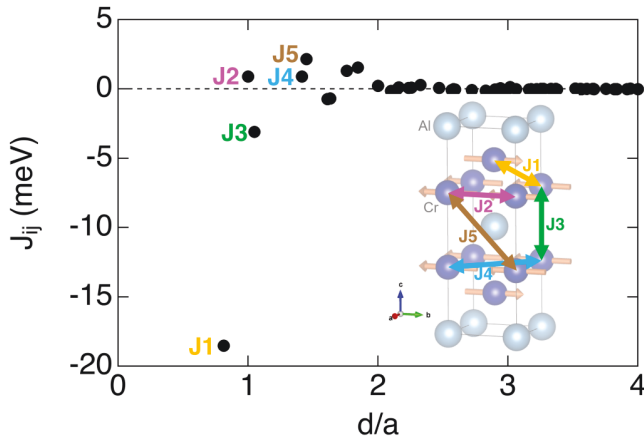

FIG. 10. Exchange coefficients J_{ij} as function of the interaction distance d (in units of the lattice parameter a) between lattice sites i and j. First- to fifth-nearest-neighbor interactions ($J1, ..., J5$) are illustrated in the subset figure with colored arrows.
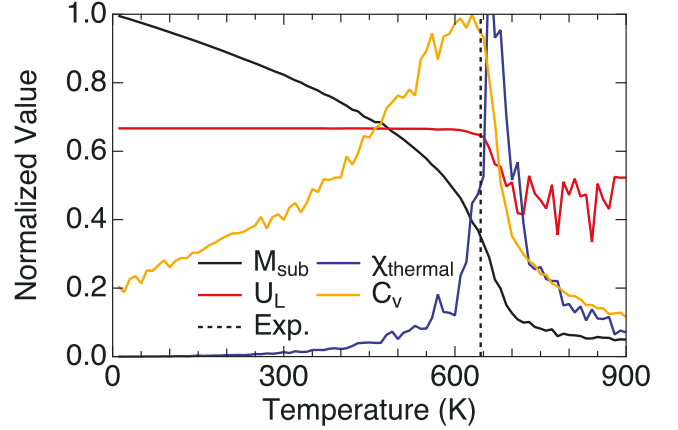

FIG. 11. Normalized sublattice magnetization and three thermodynamic observables for Cr_2Al, computed from Monte Carlo simulations of the stochastic Landau-Lifshitz-Gilbert equation. The temperature is changed using a step size of 10 K. Heat capacity C_v mirrors the heat flow while heating from DSC in Fig. 5, while the predicted T_N range is 620–670 K.

U_L, which indicates T_N as a transition from the normalized value of 0.667 to 0.444. The isothermal susceptibility $\chi_{thermal}$ and the heat capacity C_v show a peak at the critical temperature. This leads to predictions for the transition temperature of 660, 650, and 630 K, respectively, which are all in good agreement with the experimental value of 634 ± 2 K.

IV. CONCLUSIONS

Neutron diffraction and magnetometry are consistent with an in-plane magnetic structure of Cr_2Al, identical to that of Mn_2Au, but with light elements that minimize spin-orbit coupling. Magnetometry, calorimetry, and transport all confirm T_N to be 634 ± 2 K, in agreement with previous studies. The ability to access this T_N without decomposing the compound enables a more stringent test for evaluating spintronic phenomena that should vanish in the paramagnetic regime. Aligned measurements provide some early evidence for anisotropy in Cr_2Al, which will be the focus of further studies. The ability to engineer the transport and morphology, for example by thin-film deposition, should provide a promising platform for spintronic investigation.

ACKNOWLEDGMENTS

---

[1] A. V. Kimel, A. Kirilyuk, P. A. Usachev, R. V. Pisarev, A. M. Balbashov, and T. Rasing, Nature (London) **435**, 655 (2005).

[2] A. Little, L. Wu, P. Lampen-Kelley, A. Banerjee, S. Patankar, D. Rees, C. A. Bridges, J. Q. Yan, D. Mandrus, S. E. Nagler, and J. Orenstein, Phys. Rev. Lett. **119**, 227201 (2017).

[3] T. Kampfrath, A. Sell, G. Klatt, A. Pashkin, S. Mährlein, T. Dekorsy, M. Wolf, M. Fiebig, A. Leitenstorfer, and R. Huber, Nat. Photonics **5**, 31 (2011).

[4] B. Viala, G. Visentin, and P. Gaud, IEEE Trans. Magn. **40**, 1996 (2004).

[5] S. Lee, S. Grudichak, J. Sklenar, C. C. Tsai, M. Jang, Q. Yang, H. Zhang, and J. B. Ketterson, J. Appl. Phys. **120**, 033905 (2016).

[6] G. Chai, N. N. Phuoc, and C. K. Ong, Appl. Phys. Lett. **103**, 042412 (2013).

[7] V. Sharma, J. Saha, S. Patnaik, and B. K. Kuanr, AIP Adv. **7**, 056405 (2016).

[8] N. Bhattacharjee, A. A. Sapozhnik, S. Y. Bodnar, V. Y. Grigorev, S. Y. Agustsson, J. Cao, D. Dominko, M. Obergfell, O. Gomonay, J. Sinova, M. Kläui, H. J. Elmers, M. Jourdan, and J. Demsar, Phys. Rev. Lett. **120**, 237201 (2018).

[9] V. M. T. S. Barthem, C. V. Colin, H. Mayaffre, M. H. Julien, and D. Givord, Nat. Commun. **4**, 2892 (2013).

[10] M. Jourdan, H. Bräuning, A. Sapozhnik, H. J. Elmers, H. Zabel, and M. Kläui, J. Phys. D: Appl. Phys. **48**, 385001 (2015).

[11] K. Olejník, T. Seifert, Z. Kašpar, V. Novák, P. Wadley, R. P. Campion, M. Baumgartner, P. Gambardella, P. Němec, J. Wunderlich, J. Sinova, P. Kužel, M. Müller, T. Kampfrath, and T. Jungwirth, Sci. Adv. **4**, eaar3566 (2018).

[12] V. Saidl, P. Němec, P. Wadley, V. Hills, R. P. Campion, V. Novák, K. W. Edmonds, F. Maccherozzi, S. S. Dhesi, B. L. Gallagher, F. Trojánek, J. Kuneš, J. Železný, P. Malý, and T. Jungwirth, Nat. Photonics **11**, 91 (2017).

[13] P. Wadley, V. Hills, M. R. Shahedkhah, K. W. Edmonds, R. P. Campion, V. Novák, B. Ouladdiaf, D. Khalyavin, S. Langridge, V. Saidl, P. Nemec, A. W. Rushforth, B. L. Gallagher, S. S. Dhesi, F. Maccherozzi, J. Železný, and T. Jungwirth, Sci. Rep. **5**, 17079 (2015).

[14] P. Wadley, B. Howells, J. Zelezny, C. Andrews, V. Hills, R. P. Campion, V. Novak, K. Olejnik, F. Maccherozzi, S. S. Dhesi, S. Y. Martin, T. Wagner, J. Wunderlich, F. Freimuth, Y. Mokrousov, J. Kunes, J. S. Chauhan, M. J. Grzybowski, A. W. Rushforth, K. W. Edmonds *et al.*, Science **351**, 587 (2016).

[15] P. Wadley, S. Reimers, M. J. Grzybowski, C. Andrews, M. Wang, J. S. Chauhan, B. L. Gallagher, R. P. Campion, K. W. Edmonds, S. S. Dhesi, F. Maccherozzi, V. Novak, J. Wunderlich, and T. Jungwirth, Nat. Nanotechnol. **13**, 362 (2018).

[16] M. Wang, C. Andrews, S. Reimers, O. J. Amin, P. Wadley, R. P. Campion, S. F. Poole, J. Felton, K. W. Edmonds, B. L. Gallagher, A. W. Rushforth, O. Makarovsky, K. Gas, M. Sawicki, D. Kriegner, J. Zubáč, K. Olejn'ik, V. Novák, T.

[17] Jungwirth, M. Shahrokhvand *et al.*, Phys. Rev. B **101**, 094429 (2020).

[17] C. C. Chiang, S. Y. Huang, D. Qu, P. H. Wu, and C. L. Chien, Phys. Rev. Lett. **123**, 227203 (2019).

[18] S. Y. Bodnar, L. Šmejkal, I. Turek, T. Jungwirth, O. Gomonay, J. Sinova, A. A. Sapozhnik, H. J. Elmers, M. Kläui, and M. Jourdan, Nat. Commun. **9**, 348 (2018).

[19] N. Bhattacharjee, A. A. Sapozhnik, S. Y. Bodnar, V. Y. Grigorev, S. Y. Agustsson, J. Cao, D. Dominko, M. Obergfell, O. Gomonay, J. Sinova, M. Kläui, H.-J. Elmers, M. Jourdan, and J. Demsar, Phys. Rev. Lett. **124**, 039901(E) (2020).

[20] R. W. Cahn, Adv. Mater. **3**, 628 (1991).

[21] S. Khmelevskyi and P. Mohn, Appl. Phys. Lett. **93**, 162503 (2008).

[22] K. Uhlířová, E. Duverger-Nédellec, R. H. Colman, J. Volný, B. Vondráčková, and K. Carva, J. Alloys Compd. **771**, 680 (2019).

[23] M. Atoji, J. Chem. Phys. **43**, 222 (1965).

[24] B. S. Semukhin, V. M. Kushnarenko, and E. V. Kozlov, Sov. Phys. J. **31**, 267 (1988).

[25] K. Mahdouk and J.-C. Gachon, J. Phase Equilib. **21**, 157 (2000).

[26] M. Rank, P. Franke, J. Hoffmann, and H. J. Seifert, CALPHAD: Comput. Coupling Phase Diagrams Thermochem. **66**, 101638 (2019).

[27] M. A. Susner, D. S. Parker, and A. S. Sefat, J. Magn. Magn. Mater. **392**, 68 (2015).

[28] S. Calder, K. An, R. Boehler, C. R. Dela Cruz, M. D. Frontzek, M. Guthrie, B. Haberl, A. Huq, S. A. J. Kimber, J. Liu, J. J. Molaison, J. Neuefeind, K. Page, A. M. dos Santos, K. M. Taddei, C. Tulk, and M. G. Tucker, Rev. Sci. Instrum. **89**, 092701 (2018).

[29] B. H. Toby and R. B. Von Dreele, J. Appl. Crystallogr. **46**, 544 (2013).

[30] K. Momma and F. Izumi, J. Appl. Crystallogr. **41**, 653 (2008).

[31] See Supplemental Material at http://link.aps.org/supplemental/10.1103/PhysRevMaterials.5.084411 for resistivity schematic, chemical analysis, additional magnetic refinements, and total energy as a function of magnetic moment tilting, and detailed calorimetry analysis.

[32] G. Kresse and J. Furthmüller, Phys. Rev. B **54**, 11169 (1996).

[33] G. Kresse and D. Joubert, Phys. Rev. B **59**, 1758 (1999).

[34] J. P. Perdew, K. Burke, and M. Ernzerhof, Phys. Rev. Lett. **77**, 3865 (1996).

[35] P. E. Blöchl, Phys. Rev. B **50**, 17953 (1994).

[36] H. J. Monkhorst and J. D. Pack, Phys. Rev. B **13**, 5188 (1976).

[37] A. Togo and I. Tanaka, Scr. Mater. **108**, 1 (2015).

[38] S. Steiner, S. Khmelevskyi, M. Marsmann, and G. Kresse, Phys. Rev. B **93**, 224425 (2016).

[39] H. Ebert, D. Kodderitzsch, and J. Minar, Rep. Prog. Phys. **74**, 096501 (2011).

[40] A. I. Liechtenstein, M. I. Katsnelson, and V. A. Gubanov, J. Phys. F: Met. Phys. **14**, L125 (1984).

[41] O. Eriksson, A. Bergman, L. Bergqvist, and J. Hellsvik, *Atomistic Spin Dynamics: Foundations and Applications* (Oxford University Press, 2017).

[42] F. Grønvold, J. Chem. Thermodyn. **25**, 1133 (1993).

[43] K. Yang, K. Kang, Z. Diao, M. H. Karigerasi, D. P. Shoemaker, A. Schleife, and D. G. Cahill, Phys. Rev. B **102**, 064415 (2020).

[44] K. Kang, K. Yang, K. Puthalath, D. G. Cahill, and A. Schleife, arXiv:2012.02090.

[45] K. Yang, K. Kang, Z. Diao, A. Ramanathan, M. H. Karigerasi, D. P. Shoemaker, A. Schleife, and D. G. Cahill, Phys. Rev. Mater. **3**, 124408 (2019).

[46] M. H. Karigerasi, K. Kang, G. E. Granroth, A. Banerjee, A. Schleife, and D. P. Shoemaker, Phys. Rev. Mater. **4**, 114416 (2020).